

Real-time tracking of two-electron dynamics in the ionization continuum of Xe

M. Baggash and H. Rottke

Max-Born-Institut für Nichtlineare Optik und Kurzzeitspektroskopie, Max-Born-Straße 2 A, 12489 Berlin, Germany

(Received 19 March 2015; published 5 May 2015)

Real-time tracking of atomic two-electron coherent dynamics is investigated through excitation of autoionizing wave packets in the ionization continuum of xenon. Extreme-ultraviolet high-order harmonics of ultrashort Ti:Sapphire laser pulses start the wave packets in energy ranges with a dense covering by two-valence-electron and single-inner-valence-electron excited-state resonances. The 15th harmonic covers resonances of type $5s5p^6nl$ with principle quantum number n ranging from $n \approx 14$ up to $n \approx 21$ and one resonance of type $5s^25p^4nl'n'l'$ with fixed n, n' and orbital angular momenta l, l' . In parallel the 17th harmonic starts a wave packet beyond the Xe $5s5p^6$ ionization threshold where exclusively resonances contribute with two-valence electrons being excited. The evolution in time of these wave packets is probed by inducing a continuum-continuum transition with the Ti:Sapphire laser pulses at variable delay times and detecting the photoelectrons after this two-photon transition. The dependence of the experimental data on the pump-probe delay time can be approximated by a two-photon transition probability derived on the basis of Fano's theory.

DOI: [10.1103/PhysRevA.91.053403](https://doi.org/10.1103/PhysRevA.91.053403)

PACS number(s): 32.80.Zb, 42.50.Md, 32.80.Fb

I. INTRODUCTION

In a multielectron atomic system electron-electron interaction and correlation is responsible for the details of its energy level structure and the corresponding stationary wave functions (eigenstates) in the discrete as well as in the continuous part of its spectrum. Access to this interaction and correlation and therefore the wave functions can be gained either with high-resolution spectroscopy or, since the advent of ultrashort light pulses with pulse widths reaching the time domain of attoseconds, by tracking directly the evolution in time of the system after it is excited [1,2]. Two-valence- or single-inner-valence- (inner-shell-) electron excitation in a complex atom, which can give access to $e-e$ interaction and correlation, is usually found in the continuous part of the atomic energy spectrum. In photoexcitation within this energy range the interaction and correlation gives rise to characteristic resonance structures and phase shifts in the corresponding transition dipole matrix elements, which connect the continuum states to the system's ground state.

The first experiment tracking the dynamic evolution of a many-electron atom with inner-shell electrons involved in real time dealt with an Auger decay of xenon after photoionization of an inner-shell electron [3]. This experiment triggered several theoretical investigations that were concerned with Auger decay [4,5] and continuum-electron dynamics in energy ranges with Fano-resonance structures in the absorption spectrum [6–9]. Fano resonances are induced by the presence of two-electron excited states, single-inner-valence-electron excited states, or inner-shell-electron excited states, which are embedded in the ionization continuum [10]. The dynamics of an electron wave packet launched in such an energy range therefore usually involves two-electron dynamics.

Tracking electron dynamics in real time in a spectral domain where Fano resonances are observed in spectroscopic investigations has been done using mainly two experimental methods. The basis of both is launching a wave packet by excitation with an ultrashort extreme-ultraviolet (XUV) laser pulse and probing the evolution in time of this wave packet by inducing a delayed continuum-continuum transition by a

second, usually visible or infrared, laser pulse. Access to the evolution in time of the wave packet is then either gained by detecting photoelectrons, which have absorbed a pump and a probe photon [11–13] or by analyzing changes in the absorption spectrum of the XUV pulse, which are brought about by the probe pulse [14–16].

Here we are interested in the evolution in time of wave packets in the ionization continuum of xenon where the spectral range encompassed by the XUV pump pulse, which starts the wave packet, covers more than one Fano resonance. Besides an exponential decay due to autoionization we expect to observe coherences in the evolution in time of such a wave packet [8,9,13]. The wave packets in the ionization continuum of xenon are started by ultrashort high-order harmonics generated from Ti:Sapphire laser pulses. The fifteenth harmonic (H_{15} in Fig. 1) excites the atom right below the ionization threshold $5s5p^6$ ($^2S_{1/2}$) where one electron is removed from the inner-valence $5s$ shell (see Fig. 1). Here Fano resonances corresponding to Rydberg series converging at this ionization threshold contribute to the wave packet, i.e., one-electron excited states. Besides these, resonances with two-valence $5p$ -shell electrons excited are mixed into this wave packet. The seventeenth harmonic initiates a wave packet motion already well above the Xe $5s5p^6$ ($^2S_{1/2}$) ionization threshold and beyond several thresholds, where one $5p$ -valence-shell electron is removed and a second one remains in a bound, excited state of Xe^+ (Fig. 1). Within the spectrum of the harmonic H_{17} thus only Fano resonances are found, which have two-valence $5p$ electrons excited. The wave packets are tracked in time by absorption of an infrared (IR) Ti:Sapphire photon from a delayed IR pulse (Fig. 1). This creates photoelectrons, which can be isolated and detected in a kinetic energy analyzer.

With this pump-probe scheme, we are able to look into the dynamics of these wave packets in real time. Specifically, we can follow the autoionization as well as coherent two-electron dynamics that is expected to give rise to oscillatory structures on the pump-probe signal [8,13]. Our investigation has an analogy in the decay of a core-excited Rydberg wave packet, which has been studied in Ref. [17]. In what follows we will

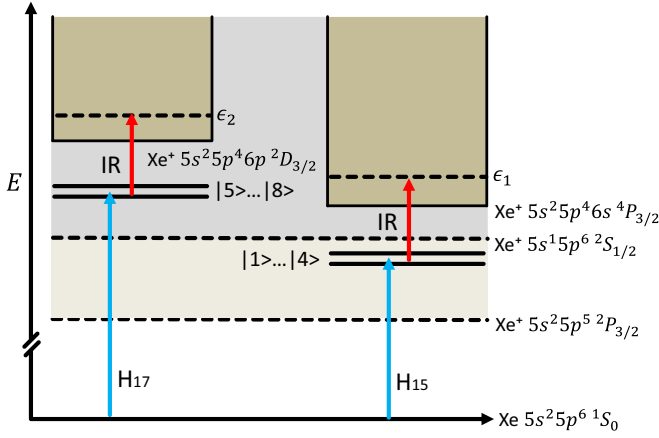


FIG. 1. (Color online) The excitation scheme used for real-time observation of two-electron dynamics. An XUV laser pulse launches a quasidiscrete wave packet in xenon with several Fano resonances participating. After a variable delay, the wave packet is probed by an IR laser pulse which induces a continuum-continuum transition to final continuum states where one photoelectron is emitted and detected and the Xe^+ ion core is left in an excited state.

first present the theoretical background necessary to analyze our experimental results, introduce the experimental setup and then describe and discuss the experimental results on the basis of known spectroscopic data in the energy ranges where we start the wave-packet dynamics.

II. THEORETICAL BACKGROUND

In the analysis of the electron dynamics we observe in the experiment we assume the XUV pump followed by the IR probe step can be addressed using second-order time-dependent perturbation theory. This is a reasonable assumption for the laser intensities we applied. The experimentally detected signal is governed by a two-photon transition matrix element $T_{f,g}(\epsilon)$ from the atomic ground state ψ_g to final continuum states $\psi_{f,\epsilon}$. The index f on $\psi_{f,\epsilon}$ is assumed to represent all discrete quantum numbers necessary to identify the final ion core and the state of the continuum electron leaving the atom. ϵ represents explicitly the kinetic energy of the photoelectron. This final continuum state $\psi_{f,\epsilon}$ is reached in two steps via an intermediate quasidiscrete wave packet, which is launched by absorption of a photon from an XUV laser pulse (Fig. 1). This wave packet is a superposition of continuum eigenstates $\psi_{j,\bar{\epsilon}}$ of the atomic Hamiltonian. We assume these intermediate continuum states can, according to Fano [10], be expressed as a linear superposition of certain discrete states ϕ_k^j and continuum states $\phi_{\bar{\epsilon}}^j$, where k is numbering the discrete

states involved:

$$\psi_{j,\bar{\epsilon}} = \sum_{k=1}^n a_k^j(\bar{\epsilon}) \phi_k^j + \int d\epsilon' b^j(\bar{\epsilon}, \epsilon') \phi_{\epsilon'}^j. \quad (1)$$

The index j represents the discrete quantum numbers necessary to identify the intermediate continuum eigenstates of the atomic Hamiltonian. $a_k^j(\bar{\epsilon})$ and $b^j(\bar{\epsilon}, \epsilon')$ are energy-dependent expansion coefficients of the atomic eigenstates $\psi_{j,\bar{\epsilon}}$ in terms of the discrete ϕ_k^j and continuum states $\phi_{\epsilon'}^j$, which are assumed to be eigenstates of a particular part of the full atomic Hamiltonian [10]. $a_k^j(\bar{\epsilon})$ and $b^j(\bar{\epsilon}, \epsilon')$ are fixed using Fano's theory to incorporate the missing part of the full Hamiltonian, which is responsible for a residual interaction among the states ϕ_k^j and $\phi_{\epsilon'}^j$ [10].

The two-photon transition matrix element from the atomic ground state ψ_g to a state $\psi_{\bar{\epsilon}}^f$ in the ionization continuum can be expressed as:

$$T_{f,g}(\epsilon) \propto \sum_j \int d\bar{\epsilon} \int_{-\infty}^{\infty} dt \int_{-\infty}^t dt' \langle \psi_{f,\epsilon} | V(t) | \psi_{j,\bar{\epsilon}} \rangle \times \langle \psi_{j,\bar{\epsilon}} | V(t') | \psi_g \rangle e^{i(\epsilon - \bar{\epsilon})t} e^{i(\bar{\epsilon} - \epsilon_g)t'}, \quad (2)$$

where an overall phase factor, which does not influence the transition probability, has been discarded. It is assumed here that only continuum intermediate states of the atom significantly contribute to $T_{f,g}(\epsilon)$. Therefore, only an integration over energies $\bar{\epsilon}$ in the ionization continuum is included in Eq. (2). The summation over j takes into account that several degenerate continua may be important. In Eq. (2) $V(t)$ represents the time-dependent interaction of the atom with the externally applied light pulses. This interaction can be written more explicitly as:

$$V(t) = (\mathbf{d}\hat{\mathbf{e}}_x)E_x(t) + (\mathbf{d}\hat{\mathbf{e}}_{\text{ir}})E_{\text{ir}}(t), \quad (3)$$

with \mathbf{d} the dipole operator of the atomic system and E_x , E_{ir} the electric fields of the XUV and IR laser pulses, respectively. $\hat{\mathbf{e}}_x$ and $\hat{\mathbf{e}}_{\text{ir}}$ are unit vectors representing the directions of linear polarization of these pulses. We will represent the electric fields of the light pulses in the form:

$$E_x(t) = A_x(t) \cos(\omega_x t), \quad (4)$$

$$E_{\text{ir}}(t) = A_{\text{ir}}(t - \delta) \cos[\omega_{\text{ir}}(t - \delta)],$$

where δ is introduced to indicate explicitly the IR laser pulse delay with respect to the XUV pulse. $A_x(t)$ and $A_{\text{ir}}(t)$ are the slowly varying amplitude functions of the electric field strengths of the pulses. ω_x and ω_{ir} are their respective carrier frequencies.

Plugging Eqs. (3) and (4) into Eq. (2) and applying the rotating wave approximation for the transition from the atomic ground state to the intermediate continuum states and for the subsequent absorption of the IR photon the transition matrix element may be rewritten as:

$$T_{f,g}^{\delta}(\epsilon) \propto \frac{1}{4} \sum_j \int d\bar{\epsilon} \underbrace{\langle \psi_{f,\epsilon} | \mathbf{d}\hat{\mathbf{e}}_{\text{ir}} | \psi_{j,\bar{\epsilon}} \rangle \langle \psi_{j,\bar{\epsilon}} | \mathbf{d}\hat{\mathbf{e}}_x | \psi_g \rangle}_{P_a^{f,j}(\epsilon, \bar{\epsilon})} e^{-i\bar{\epsilon}\delta} \underbrace{\int_{-\infty}^{\infty} dt \int_{-\infty}^t dt' e^{i(\epsilon - \bar{\epsilon} - \omega_{\text{ir}})t} e^{i(\bar{\epsilon} - \epsilon_g - \omega_x)t'} A_{\text{ir}}(t) A_x(t')}_{P(\epsilon, \bar{\epsilon}, \delta)}, \quad (5)$$

where again an overall phase factor has been discarded. The superscript δ on the transition matrix element is added to indicate its explicit dependence on the delay between the XUV and IR laser pulses. In $T_{f,g}^\delta(\epsilon)$ in Eq. (5) two factors enter the integral over the intermediate-state energies $\tilde{\epsilon}$. One, depending only on the characteristics of the atom, consists of the product of atomic dipole matrix elements [$P_a^{f,j}(\epsilon, \tilde{\epsilon})$ in Eq. (5)], and a second one, which depends only on the characteristics of the laser pulses [$P_l(\epsilon, \tilde{\epsilon}, \delta)$ in Eq. (5)]. The effect of the delay of the IR pulse with respect to the XUV one appears as a phase factor $\exp(-i\tilde{\epsilon}\delta)$ in Eq. (5), which depends on the intermediate continuum state energy $\tilde{\epsilon}$.

$P_a^{f,j}(\epsilon, \tilde{\epsilon})$, the product of atomic dipole matrix elements, can be further evaluated using Fano's theory [10]. We assume that the relevant Fano resonances within the spectral bandwidth of the XUV laser pulse can be represented by continuum wave functions as given in Eq. (1) with n discrete states involved, which have a residual interaction with one continuum and possibly among each other. Further on we assume that the final continuum, reached after absorption of the IR photon, is free of Fano resonances in the relevant spectral range and the continuum-continuum dipole matrix element in $P_a(\epsilon, \tilde{\epsilon})$ can be approximated by:

$$\langle \psi_{f,\epsilon} | \mathbf{d}\hat{\mathbf{e}}_{\text{ir}} | \psi_{j,\tilde{\epsilon}} \rangle = \sum_{k=1}^n a_k^j(\tilde{\epsilon}) \langle \psi_{f,\epsilon} | \mathbf{d}\hat{\mathbf{e}}_{\text{ir}} | \phi_k^j \rangle, \quad (6)$$

that is, only the discrete states in the expansion of the atomic continuum intermediate states $\psi_{j,\tilde{\epsilon}}$ in Eq. (1) make a relevant contribution. This is a reasonable assumption in our experimental situation. Based on these assumptions $P_a^{f,j}(\epsilon, \tilde{\epsilon})$ can be shown to have the general form:

$$P_a^{f,j}(\epsilon, \tilde{\epsilon}) = D^j \left(\sum_{k=1}^n \frac{p_k^j}{E_k^j} \right) \frac{1 + \sum_{k=1}^n \frac{q_k^j}{E_k^j}}{1 + \left(\sum_{k=1}^n \frac{1}{E_k^j} \right)^2}, \quad (7)$$

with only a few parameters determining the dependence of the product of dipole matrix elements on the intermediate and final state energies. The energies E_k^j are given by $E_k^j = (\tilde{\epsilon} - \epsilon_k^j) / \Gamma_k^j / 2$ with ϵ_k^j representing the position of the k th resonance and Γ_k^j its width. The q_k^j represent Fano q parameters, which depend on the transition dipole matrix elements from the atomic ground state to the intermediate discrete states ϕ_k^j and to the continuum states ϕ_ϵ^j [see Eq. (1)]. D^j is the dipole matrix element for the transition from the ground to the intermediate continuum ϕ_ϵ^j (see Ref. [10]). The parameters p_k^j are related to the matrix elements $\langle \psi_{f,\epsilon} | \mathbf{d}\hat{\mathbf{e}}_{\text{ir}} | \phi_k^j \rangle$ which enter the continuum-continuum dipole matrix element in Eq. (6). For our purposes all the parameters are assumed to be independent of the intermediate- and final-state energies over the spectral widths covered by the XUV and IR laser pulses, respectively.

Equation (7) obviously shows that individual resonances do not enter $P_a^{f,j}(\epsilon, \tilde{\epsilon})$ via a simple sum over individual Fano resonances. This is similar to the bound-continuum absorption cross section for the same situation [10]. Only in case the individual resonances are well separated, meaning their separations $|\epsilon_k^j - \epsilon_l^j|$ are large compared to their widths

Γ_k^j , $P_a^{f,j}(\epsilon, \tilde{\epsilon})$ can be approximated by such a sum as can be seen in Eq. (7). As a function of the intermediate-state energy $\tilde{\epsilon}$ $P_a^{f,j}(\epsilon, \tilde{\epsilon})$ has n pairs of pairwise complex conjugate poles in the complex plane, off the real axis. Each pair is representable by $\tilde{\epsilon}_k^j \pm i\tilde{\Gamma}_k^j/2$, $k = 1, 2, \dots, n$ ($\tilde{\Gamma}_k^j > 0$). Generally the $\tilde{\epsilon}_k^j$ and the $\tilde{\Gamma}_k^j$ will be different from the width Γ_k^j and resonance position ϵ_k^j parameters entering $P_a^{f,j}(\epsilon, \tilde{\epsilon})$ in Eq. (7). Only in the case of energetically well-separated resonances (see above) they will tend to be equal.

For all reasonable laser pulses $P_l(\epsilon, \tilde{\epsilon}, \delta)$ in Eq. (7) can be assumed to be an analytic function of the intermediate-state energy $\tilde{\epsilon}$ with the additional characteristics that, for the delay δ being larger than zero, $P_l(\epsilon, \tilde{\epsilon}, \delta)$ approaches zero for $|\tilde{\epsilon}| \rightarrow \infty$ faster than $1/|\tilde{\epsilon}|$ in the lower complex plane ($\text{Im } \tilde{\epsilon} \leq 0$). Under these circumstances the integral over intermediate-state energies in Eq. (5) can be evaluated analytically by calculating the residues of the integrand at the poles of $P_a^{f,j}(\epsilon, \tilde{\epsilon})$ in the lower complex plane. Provided $P_a^{f,j}(\epsilon, \tilde{\epsilon})$ has only simple poles the two-photon transition matrix element $T_{f,g}^\delta(\epsilon)$ can be represented by:

$$T_{f,g}^\delta(\epsilon) \approx \frac{1}{4} \sum_j \sum_{k=1}^n a_k^j(\epsilon) \exp[-i\delta(\tilde{\epsilon}_k^j - i\tilde{\Gamma}_k^j/2)], \quad (8)$$

with the time delay δ being larger than zero, i.e., the IR pulse follows the XUV pulse. The delay time only appears in the exponential functions entering the sum thus giving rise to each summand consisting of the product of an oscillatory term $\exp(-i\tilde{\epsilon}_k^j\delta)$ and a term $\exp(-\tilde{\Gamma}_k^j\delta)$ decreasing exponentially with the delay time due to finite resonance lifetimes. Based on Eq. (8) the general form of the two-photon transition probability to a final continuum state becomes:

$$\begin{aligned} |T_{f,g}^\delta(\epsilon)|^2 \approx & \sum_{\alpha=1}^M b_{\alpha,\alpha}(\epsilon) \exp(-\tilde{\Gamma}_\alpha\delta) + \sum_{\substack{\alpha,\beta=1 \\ \alpha < \beta}}^M b_{\alpha,\beta}(\epsilon) \\ & \times \cos[(\tilde{\epsilon}_\alpha - \tilde{\epsilon}_\beta)\delta + \phi_{\alpha,\beta}(\epsilon)] \exp[-(\tilde{\Gamma}_\alpha + \tilde{\Gamma}_\beta)\delta/2] \end{aligned} \quad (9)$$

with the double sum in Eq. (8) suitably renumbered. The $\tilde{\Gamma}_\alpha$ are twice the imaginary and the $\tilde{\epsilon}_\alpha$ the real parts of the poles of $P_a^{f,j}(\epsilon, \tilde{\epsilon})$ in Eq. (7). The $b_{\alpha,\beta}(\epsilon)$, which may be assumed to be positive valued, are functions of the final-state energy. They peak close to the final-state energy $\epsilon = \epsilon_g + \omega_x + \omega_{\text{ir}}$ with ϵ_g the ground-state energy of the atom. The $b_{\alpha,\beta}(\epsilon)$ are linked to the complex amplitudes $a_k^j(\epsilon)$ in Eq. (8). Similarly, the energy-dependent phases $\phi_{\alpha,\beta}(\epsilon)$ are determined by these complex amplitudes.

The first sum on the right-hand side of Eq. (9) can be interpreted to represent a population loss of bound states due to autoionization. The corresponding rates are related to the imaginary parts of the poles of $P_a^{f,j}(\epsilon, \tilde{\epsilon})$. The damping of the amplitudes of the oscillating contributions to the second sum may be thought of as a loss of coherence in the coherent bound wave-packet motion due to this autoionization. The rate of this loss of coherence is proportional to the sum of the amplitude decay rates $(\tilde{\Gamma}_\alpha + \tilde{\Gamma}_\beta)/2$ of the corresponding bound states involved.

It is this expression (9) for the delay dependence of the two-photon ionization probability we will use to analyze and approximate the experimental data, with the parameters entering Eq. (9) used as adjustable values (see also Ref. [13]). Being more specific, we use

$$S(\delta) = \int d\epsilon |T_{f,g}^{\delta}(\epsilon)|^2, \quad (10)$$

where the integration is done over the whole range of kinetic energies where photoelectrons are found after the two-photon absorption. A relation similar to Eq. (9), characterizing the delay dependence of photoelectron spectra, has been derived using the strong-field approximation for the interaction of the IR laser pulse with the atom in Ref. [8].

As a final remark it has to be pointed out that relation (8), with the delay time δ only appearing in the exponential function, is a consequence of the poles of $P_a^{f,j}(\epsilon, \tilde{\epsilon})$ [relation (7)] being simple ones. In case $P_a^{f,j}(\epsilon, \tilde{\epsilon})$ comprises a higher-order pole the corresponding exponential function in (8) gets multiplied by a polynomial in the delay time δ of the order of this pole minus one. This will have a significant effect on the dependence of the two-photon transition probability (9) on the time delay δ . It may, for example, result in a delayed development of a maximum in $|T_{f,g}^{\delta}(\epsilon)|^2$ as a function of δ .

III. EXPERIMENTAL SETUP

The scheme of the experimental setup is shown in Fig. 2. The experiment has been performed using a 1 kHz repetition rate Ti:Sapphire laser system (Spectra Physics, Spitfire Pro) delivering pulses with a width of 42 ± 5 fs and 2.6 mJ energy at 798 nm carrier wavelength. As has been described in detail in Ref. [18] the laser beam was split into two parts, a central and an annular one, which were sent to two separate arms of a delay line and then recombined again. The central part of the beam, carrying ≈ 2 mJ of pulse energy, served to generate high-order harmonics. The annular part, with a pulse energy of up to $\approx 15 \mu\text{J}$, was used as probe beam inducing the continuum-continuum transition in the atomic species investigated. The coarse delay of the laser pulses with respect to each other was set by a mirror on a translation stage, while the fine tuning and the systematic scan of the time delay was done by a fused silica wedge pair in one of the delay line arms. The maximum delay

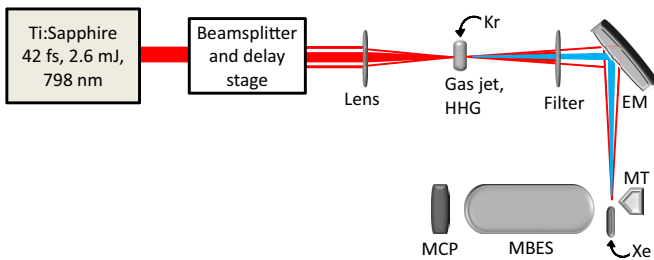


FIG. 2. (Color online) Scheme of the experimental setup. HHG: high-order-harmonic generation, EM: elliptic, grazing incidence, gold-coated mirror for imaging the source point of the high-order harmonics to the interaction point with the xenon gas, MBES: magnetic bottle time-of-flight spectrometer with MT the solid-state magnet, MCP: microchannel plate stack for photoelectron detection.

achievable with this wedge pair was 1100 fs. Measurements presented here were performed using delay time scans with a step width of 8.2 fs and a data acquisition time of 250 s for every time delay.

High-order harmonics were generated in Kr gas (see Ref. [18]). From the generated harmonics, only the 11th and harmonics of higher order passed through an aluminum filter foil (thickness: 300 nm) positioned downstream of the harmonic source. This filter also blocked the Ti:Sa laser pulses used for high-order-harmonic generation (HHG). The annular Ti:Sa laser beam from the second arm of the delay line passed around this aluminum filter. The collinear propagating infrared and harmonic beams were then focused on the target gas using a grazing incidence gold-coated elliptical mirror.

Of the harmonics passing the Al filter only the 15th and 17th, with photon energies 23.31 eV and 26.41 eV, respectively, started the wave packets in the ionization continuum of the target gas we were interested in here. The bandwidths of these individual harmonics were approximately 100 meV as estimated from the measured width of photoelectron kinetic energy distributions from photoionizing xenon gas with these harmonics.

The xenon target gas was supplied as an effusive beam from a capillary, positioned close to the focal spot of the harmonic and infrared laser beams. The effusive beam crossed the laser beams at right angles. The directions of polarization of the harmonic and infrared beams were chosen to be parallel. Photoelectrons created in the focal spot were energy analyzed in a magnetic bottle time-of-flight spectrometer and detected using a pair of chevron stacked multichannel plates (MCP) [18]. The signal from the MCP stack was fed into an averaging transient digitizer, which recorded the time-of-flight spectrum of the photoelectrons. Since we used a magnetic bottle spectrometer any information on the direction of emission of the photoelectrons is lost.

IV. RESULTS AND DISCUSSION

A. Fano resonances involved in the quasidiscrete wave packets

Examining the photoelectron kinetic energy distributions after interaction of the Xe target gas with the high-order-harmonic extreme ultraviolet (XUV) and the infrared (IR) laser pulses we find two distinct ranges of kinetic energy where the photoelectron yield depends significantly on the delay of the IR pulses with respect to the XUV ones. These energy ranges are shown in Figs. 3(a) and 3(b), respectively, for two delay times, one ($\delta = -172$ fs) where the IR pulses precede the XUV ones and one [$\delta = 50$ fs, Fig. 3(a); $\delta = 74$ fs, Fig. 3(b)] where the IR follow the XUV pulses. With the IR following the XUV pulses a clear enhancement of the photoelectron yield is observable. The energy scale in these spectra, and therefore the kinetic energy ranges where we observe the photoelectron yield enhancement, is estimated to be correct to within $\Delta E \approx \pm 50$ meV.

The XUV radiation passing through the interaction region with the Xe atoms consists of the harmonics 11 through 19 of the IR radiation. The corresponding photon energies are located between 17.09 eV (harmonic H_{11}) and 29.51 eV (H_{19}). The intensity of the harmonic H_{19} is already very

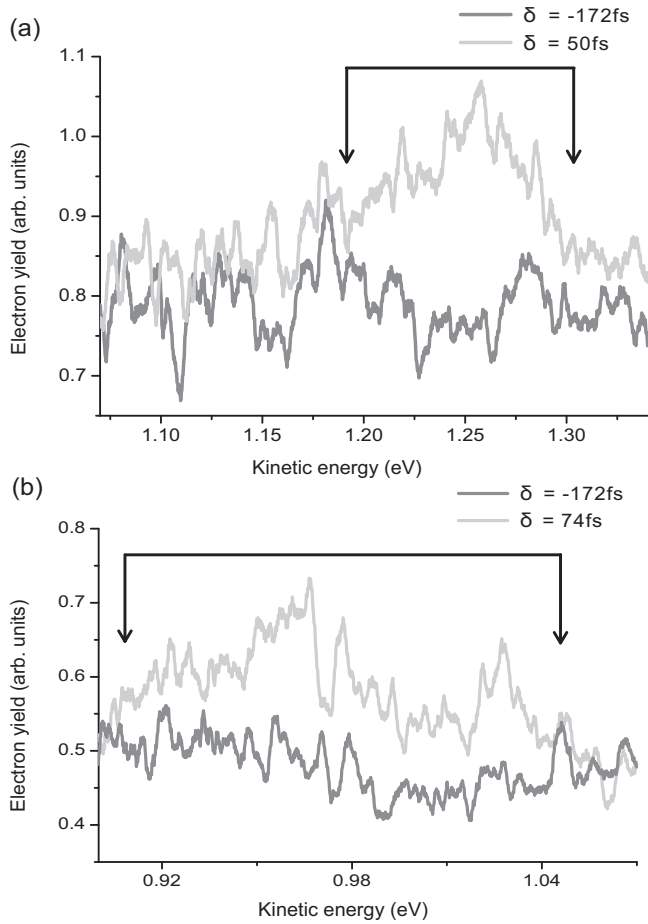


FIG. 3. Two sections of the photoelectron kinetic energy distribution showing the energy ranges, where we detect photoelectrons from two-photon ionization of xenon by absorption of one harmonic H_{15} followed by one infrared photon (a) and by absorption of one H_{17} followed by one IR photon (b). Both distributions, (a) and (b), are shown at two delay times of the IR relative to the harmonic pulses [black curves: at a delay $\delta = -172$ fs; gray curves: (a) for $\delta = 52$ fs, (b) for $\delta = 74$ fs]. For the positive delay times the IR follow the harmonic pulses.

weak. We expect that it will not contribute significantly to the photoelectron spectrum in the range of low kinetic energies relevant to this experiment. Significant contributions are only expected from H_{11} – H_{17} . Photoionization of Xe by these harmonics with the Xe^+ ion core left in the lowest-lying electronic states $5s^25p^5(^2P_{3/2}, ^2P_{1/2})$ does not contribute to the low kinetic energy photoelectron spectra shown in Figs. 3(a) and 3(b). The photoelectrons in these main ionization channels of Xe have a significantly higher kinetic energy due to the small ionization potentials involved, namely 12.13 eV and 13.44 eV, respectively [20]. Similarly, one-photon ionization by the harmonic H_{17} leaving the Xe^+ ion core in a state with one electron removed from the $5s$ shell, i.e., with an electron configuration $5s5p^6$, also does not contribute to the photoelectron spectra in Figs. 3(a) and 3(b). The corresponding ionization potential is 23.4 eV [20]. Thus, these photoelectrons would have a kinetic energy of ≈ 3 eV. However, one-photon ionization by the harmonic H_{17} with the Xe^+ ion left in

TABLE I. Xenon resonances found within the bandwidths of the 15th (resonance numbers 51, . . . , 58) and 17th harmonics (resonance numbers 141, . . . , 144). Their energies, electron configurations and resonance identification numbers are taken from Ref. [19]. Not all resonances have been identified up to now.

no.	Configuration	J	Energy (eV)
51	$5s5p^6(^2S_{1/2})14p$	1	23.272
52		1	23.301
53		1	23.313
54	$5p^4(^3P)6s(^4P_{3/2})10p$	1	23.333
55	$5s5p^6(^2S_{1/2})19p$	1	23.340
56		1	23.347
57	$5s5p^6(^2S_{1/2})21p$	1	23.352
58	$5s5p^6(^2S_{1/2})22p$	1	23.357
141	$5p^4(^3P)6p(^4D_{3/2})10d$	1	26.354
142	$5p^4(^3P)6p(^4D_{3/2})11d$	1	26.413
143	$5p^4(^3P)6p(^4D_{3/2})12d$	1	26.454
144	$5p^4(^3P)6p(^4D_{3/2})13d$	1	26.484

excited states with electron configurations $5s^25p^4nl$, where one electron is removed from the $5p$ shell and a second one is left in an excited bound orbital (nl), may contribute to the photoelectron spectra in Figs. 3(a) and 3(b). Possible excited orbitals nl contributing are $6s$, $5d$, and $6p$. In the energy interval between the $5s5p^6$ ionization threshold at 23.4 eV and the photon energy of the harmonic H_{17} (26.41 eV) there are many Xe ionization thresholds found, which are based on these Xe^+ electron configurations [20]. Just these thresholds are responsible for a significant background photoelectron yield we find in Figs. 3(a) and 3(b) spread out over the whole spectra when the IR laser pulses precede the XUV ones. The photon energy of the harmonic H_{15} is just right below the $5s5p^6$ ionization threshold, which is the lowest one beyond the thresholds $5s^25p^5(^2P_{3/2}, ^2P_{1/2})$. It thus does not contribute low kinetic energy photoelectrons.

The photoelectron yield enhancement in Fig. 3(a) (kinetic energy interval: ≈ 1.2 eV – ≈ 1.3 eV), when the IR follow the XUV pulses, is generated by the absorption of one XUV and one IR photon. It depends on the delay time between these pulses. Moreover, the yield enhancement critically depends on the intensity of the harmonic H_{15} . It maximizes when we maximize the H_{15} intensity by adjusting the harmonic generation for optimum H_{15} output even if the harmonic H_{17} is generated at a reduced level. We thus may attribute this enhancement to the absorption of one H_{15} photon followed by the absorption of an IR photon.

The center photon energy of the harmonic H_{15} (23.31 eV) is only slightly (100 meV) lower than the ionization threshold that leaves the Xe^+ ion in the lowest excited electron configuration $5s5p^6$ (23.4 eV) where one electron is removed from the $5s$ inner-valence orbital. Within the bandwidth of this harmonic several Fano resonances are found (Table I). We have listed in Table I all resonances within this bandwidth, which have been observed experimentally in Ref. [19], the only high-resolution measurement of the Xe absorption cross section close to the $5s5p^6$ ionization threshold available. The resonance numbering in the first column of the table is taken from [19]. Sukhorukov *et al.* have recently made

a theoretical analysis of these resonances [21] in an energy range partly covering the range where the harmonic H_{15} excites the Xe atom. Except for three (numbers 52, 53, and 56) all but one of the remaining resonances, that have been identified, belong to a Rydberg series $5s5p^6(^2S_{1/2})np$, which converges at the ionization threshold $5s5p^6(^2S_{1/2})$. The principal quantum numbers n involved range from $n = 14$ up to $n \approx 21$. Only those with $n = 14, 19 - 21$ have actually been identified using experimental data [19]. They are listed in Table I. The position of the other resonances of this Rydberg series within the bandwidth of H_{15} can only be estimated using the quantum defects of the known members of this series [19,21]. The assignment made to the Fano resonance with identification number 54 in Table I can only be viewed as being tentative [19,21]. For the resonances with nos. 52, 53 and 56 there has been no assignment possible up to now.

Absorption of an IR photon of the quasidiscrete wave packet started by the harmonic H_{15} , which encompasses the Fano resonances introduced in the previous paragraph, gives rise to the photoelectrons observed with a kinetic energy centered at ≈ 1.25 eV in Fig. 3(a) with an energy spread of $\approx \pm 50$ meV. This kinetic energy excludes the Xe^+ excited state $5s5p^6(^2S_{1/2})$ from being the corresponding ionization threshold. The Xe ionization threshold, which would give rise to photoelectrons in the kinetic energy range where we observe them corresponds to the Xe^+ excited state $5s^25p^4(^3P)6s(^4P_{5/2})$ using the notation of Ref. [21]. Since we do not observe photoelectrons after two-photon absorption with a kinetic energy, which would correspond to $5s5p^6(^2S_{1/2})$ being the ionization threshold we may conclude that the Fano resonances corresponding to the Rydberg series $5s5p^6(^2S_{1/2})np$ ($n = 14, \dots, 21$) do play a minor role in the two-photon ionization process of Xe with the harmonic H_{15} involved. As will be seen below the observed evolution in time of the wave packet may support this conclusion.

With arguments similar to those presented above we are able to attribute the photoelectron yield enhancement found in Fig. 3(b) for the IR pulses following the XUV ones to the absorption of one harmonic H_{17} photon followed by one IR photon. The harmonic H_{17} (photon energy 26.41 eV) starts a quasidiscrete wave packet in an energy range already significantly higher than the Xe ionization threshold $5s5p^6(^2S_{1/2})$ at 23.4 eV. Within the bandwidth of H_{17} we therefore find Fano resonances corresponding to Rydberg series where two electrons are excited and which are converging to ionization thresholds $5s^25p^4nl$ with $nl = 5d$ or $n \geq 6$. According to Ref. [19] four Fano resonances are expected to be found in the spectral range of H_{17} . They are also listed in Table I and are numbered 141–144 in the first column of the table, again according to the resonance numbering in Ref. [19]. Codling and Madden tentatively assigned these resonances to be members of a Rydberg series $5s^25p^4(^3P)(6p)(^4D_{3/2})nd$ with the principal quantum numbers n ranging from 10–13 and ionization limit $5s^25p^4(^3P)6p(^4D_{3/2})$ at 26.61 eV [19]. At this energy [20,22] locate the ionization threshold $5s^25p^4(^3P_2)6p(^2P_{3/2})$. Thus, the resonances more reasonably may be assigned to a Rydberg series $5s^25p^4(^3P_2)6p(^2P_{3/2})nd$.

The kinetic energy of the photoelectrons after two-photon absorption of one H_{17} and one IR photon is

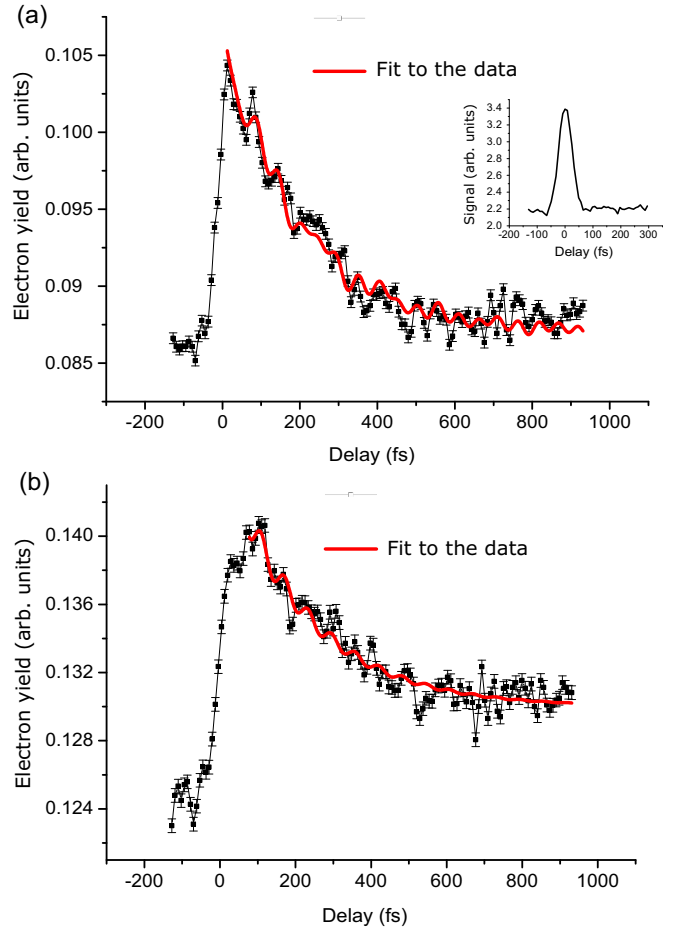


FIG. 4. (Color online) (a) and (b) show the measured dependences of the photoelectron yields in the photoelectron kinetic energy ranges between the markers in Figs. 3(a) and 3(b), respectively, on the delay of the IR with respect to the harmonic H_{15} (a) and H_{17} (b) pulses. The black-dotted lines with the error bars represent the experimental data. The red lines represent fit curves, which are based on the equations (9) and (10). A positive delay means the IR follow the XUV pulses. The inset in (a) shows an IR-XUV cross-correlation curve, which was used to determine the zero point of the time delay. It also indicates the time resolution limit.

spread over an energy range from ≈ 0.92 eV to ≈ 1.03 eV [Fig. 3(b)]. This allows two excited Xe^+ final states to be the final ionization channels after two-photon absorption. They are the states $5s^25p^4(^3P_0)6p^2[1]^0$, $J = 1/2$ and $5s^25p^4(^1D_2)5d^2[3]$, $J = 5/2$ (notation according to [20]) with the corresponding Xe ionization potentials being 27.06 eV and 26.89 eV, respectively [20,23]. Both of them may contribute to the photoelectron yield we observe.

B. Evolution in time of the wave packets

Figures 4(a) and 4(b) show the dependence of the photoelectron yields, integrated over the kinetic energy ranges marked in Figs. 3(a) and 4(b), respectively, on the time delay of the IR with respect to the high-order harmonic pulses. Zero delay time corresponds to the optimum overlap in time of the XUV and IR pulses. It was determined in the same measurement by

recording the cross correlation of the IR and harmonic pulses. The cross correlation is directly accessible via photoelectron sidebands, which are generated by absorption of one harmonic photon followed by one IR photon absorption or stimulated emission in the main Xe photoionization channel where one electron is removed from the $5p$ orbital [24]. The inset in Fig. 4 shows the cross correlation curve. Positive delay times in Fig. 4 mean the IR pulses follow the harmonic pulses. In both Figs. 4(a) and 4(b) the black connected dots with the error bars represent the respective measured photoelectron yields corresponding to the absorption of one H_{15} and one IR photon [Fig. 4(a)] or one H_{17} followed by one IR photon [Fig. 4(b)].

Both Figs. 4(a) and 4(b) show similar characteristic features in the delay time interval covered by the experiment. The photoelectron yield reaches a maximum slightly delayed with respect to time zero, with this delay being somewhat larger in Fig. 4(b). The rise of the yield at zero delay is also slightly less steep in Fig. 4(b) than it is in 4(a). The maximum is followed by a mean decrease of the yield with increasing time delay in a time interval up to ≈ 600 fs. On the average the photoelectron yield then becomes constant up to the largest accessible delay at a level that is significantly higher than the background level, specifically in Fig. 4(b). The quite high background level of photoelectrons can be discerned in the figures for negative time delays where the IR precede the harmonic pulses. As explained in the previous section these background photoelectrons are generated by one-photon ionization of Xe by harmonics of order larger than H_{15} present in the beam. One further feature observable is an oscillatory structure superimposed on the overall monotonic decrease of the yield with the time delay. As the figures show, the amplitude of this structure is larger than the noise level, represented by the error bars. This oscillatory structure is caused by the coherent evolution in time of the wave packets started by the harmonics H_{15} and H_{17} , respectively, in the ionization continuum due to the presence of Fano resonances within their spectral widths [see Eq. (9) above for the expected dependence of the ionization probability on the pump-probe time delay]. The shortest oscillation period one would expect to find in the experiment corresponds to the largest energy difference between Fano resonances within the bandwidth of the respective harmonic. This difference approximately corresponds to the bandwidth of the individual harmonics of ≈ 100 meV. From this bandwidth one derives ≈ 40 fs for this period. This value is practically equal to the width of the IR laser pulses, which sets the lower limit to the oscillation period, which should be resolvable in the experiment.

A crucial prerequisite to detect the evolution in time of the full wave packet started by the harmonic pulses H_{15} and H_{17} , respectively, is the existence of at least one final continuum state, which can be reached after absorption of the IR probe photon with comparable probabilities from all of the Fano resonances of the Xe atom, which contribute to the formation of the wave packet. If this is not granted, or the contribution of such a final state to the whole two-photon transition probability is small, the coherent contributions to the overall transition probability will be largely suppressed, and thus also the visibility of the corresponding coherent evolution in time of the wave packet [see Eq. (9)]. If only part of the Fano resonances, which make up the wave packet, contribute to the transition to one final state, only the coherent evolution in time

of this part of the whole wave packet can be observed in the pump-probe experiment. In our experiment we only restrict the kinetic energy of the photoelectrons contributing to the pump-probe signal. Thus, a possibly significant number of different degenerate final continuum eigenstates will contribute to the measured signal. These facts may be responsible for the smallness of the oscillatory structures, which map the coherent evolution in time of the wave packet, we find in the experiment. The main feature is a mean exponential decay of the pump-probe signal, which represents a mere population decay [the first sum on the right-hand side of Eq. (9)] due to autoionization of the Fano resonances involved in the quasidecrete wave packet started by the XUV pulse.

The large number of Fano resonances found within the spectral bandwidths of the harmonics H_{15} and H_{17} according to previous spectroscopic investigations (Table I) and their incomplete characterization hamper a full analysis of the evolution in time of the wave packets. The basis for our analysis below is Eq. (10) above, i.e., the two-photon transition probability [Eq. (9)] integrated over the final spectral range where we detect the photoelectrons. To facilitate an analysis we will make several simplifying assumptions. We will assume that the phases $\phi_{\alpha,\beta}(\epsilon)$ appearing in the transition probability [Eq. (9)] do not depend on the final-state energy ϵ , i.e., the kinetic energy of the photoelectrons. They are replaced by mean values, which will be used as fit parameters. A second set of fit parameters will then be the amplitudes $b_{\alpha,\beta}(\epsilon)$ in Eq. (9) integrated over the respective spectral ranges where we detect the photoelectrons.

The experimental findings [Figs. 4(a), 4(b)], i.e., the course of the delay time dependence of the photoelectron yields, suggest two differing population decay rate ranges being involved: a range of high rates, which gives rise to the initial decrease of the yield within the time range investigated, and a second one, with small rates, which gives rise to the residual photoelectron yield for large delay times. As a starting point we use a single rate constant to fit the initial mean decay of the experimental photoelectron yields in Figs. 4(a), 4(b). The best fit to the data is found with $\Gamma = 5.0 \pm 0.15 \text{ ps}^{-1}$ [Fig. 4(a)] and $\Gamma = 4.6 \pm 0.2 \text{ ps}^{-1}$ [Fig. 4(b)]. Trying to improve the fit by using two independently variable rate constants resulted in values for the two rates, which differ by less than the error limits we get from the fitting procedure. This means that to within our experimental accuracy, the data are reasonably well represented by one rate constant for the initial mean decay of the photoelectron yield.

The wave packet started by the harmonic H_{15} encompasses contributions from Fano resonances attributable to the Rydberg series $5s5p^6 ({}^2S_{1/2})np$ with $n = 14, \dots, 21$ (see Table I). The decay rates of these resonances may be extrapolated from known values for smaller principal quantum numbers using the relation $\Gamma(n^*)^3 \approx \text{const.}$, which may be applicable [25]. Here n^* is the effective principal quantum number of the respective resonance. This relation would not be applicable in case the higher n members of this Rydberg series are perturbed by other resonances. Based on $\Gamma(n^*)^3 \approx \text{const.}$ and the Xe data of Ref. [25] one gets $\Gamma \approx 0.72 \text{ ps}^{-1}$ for the $n = 14$ member of the Rydberg series and correspondingly smaller decay rates for the higher n members. These estimated rates are significantly smaller than the one we found for the fast photoelectron yield

decay in Fig. 4(a). Despite the fact that the difference of these rate constants and the one determined above is significantly larger than the error limits we got from the fitting routine a corresponding population decay cannot be retrieved from the data. We suspect the main reason for this being the smallness of the population of the resonances $5s5p^6(^2S_{1/2})np$ with $n = 14, \dots, 21$. This would be in accordance with the small residual photoelectron yield enhancement found towards the end of the delay range investigated.

We fit the oscillatory, coherent contribution to the photoelectron yield in Fig. 4(a) in a second step, with the second sum on the right-hand side of Eq. (9). This can only be done tentatively. Only one fast population decay rate constant Γ was identified. However, there are four resonances this rate constant may be attributed to (respectively, numbers 52–54, 56 in Table I). A Fourier transform of the photoelectron yield with respect to the delay time suggests four frequencies to contribute mainly to the oscillatory structure in a range $0.0045 \text{ fs}^{-1} \leq \nu \leq 0.025 \text{ fs}^{-1}$. The lower frequency limit is set by a steep rise of the magnitude of the Fourier transform towards $\nu = 0$, which masks possible oscillation frequencies in the range $\nu < 0.0045 \text{ fs}^{-1}$, and the upper limit by the bandwidth of the laser pulses that are involved. The identifiable oscillation frequencies closely resemble corresponding energy differences between pairs of Fano resonances with numbers 54 and 51, 57 and 54, 58 and 54, and 58 and 51 (see Table I for the resonance numbering). More information on possible further resonance pairs contributing to the oscillatory structure in the experimental data for the wave packet started by the harmonic H_{15} cannot be inferred from these data. This result indicates that the high population decay rate constant may be attributed to the resonance number 54 with two $5p$ -shell electrons excited. Assuming now $\Gamma(n^*)^3 = 0.81 \text{ fs}^{-1}$ (see Ref. [25]) for the resonances with one $5s$ -shell electron excited (see the discussion above) the best fit of Eq. (9) to the experimental data, based on the resonance pairs mentioned above, is represented by the red, solid curve in Fig. 4(a). It reproduces the course of the experimental data quite reasonably, specifically in the first half of the delay range. The main contribution to the appearance of an oscillatory structure on the fit curve towards the end of the delay range stems from the 58-51 resonance pair with both resonances being members of the Rydberg series with one $5s$ -shell electron excited. For this pair the coherence decay rate $(\Gamma_{58} + \Gamma_{51})/2$ is small.

The analysis of the experimental data above indicates that the coherent evolution in time of the wave packet started by the harmonic H_{15} in the ionization continuum is mapped at least partly into the photoelectron yield detected in the pump-probe experiment after absorption of one XUV pump and one IR probe photon. This means that there are common final continuum states reached by pathways via at least part of the Fano resonances, which contribute to the wave packet. This does not mean that those resonances, which did not enter the fitting procedure do either not contribute to the wave packet (i.e., are not excited by H_{15}) or do not at all allow to reach the same final state after two-photon absorption to be visible as a coherent contribution to the photoelectron yield. The present quality of the experimental data we have been able to achieve and the limited delay range basically do not allow to retrieve their possible contribution yet.

For the wave packet started by the harmonic H_{17} we also have been able to identify only one population decay rate constant $\Gamma = 4.6 \pm 0.2 \text{ ps}^{-1}$, which reproduces the fast decrease of the photoelectron yield. Spectroscopy data indicate that Fano resonances contributing to this wave packet belong to one Rydberg series with $n = 10, \dots, 13$, nothing else is known in this spectral range (see Table I) [19,23]. In order to analyze a possible coherent contribution to the photoelectron yield we will assume that only these resonances contribute to the wave packet and all have the same decay rate constant $\Gamma = 4.6 \text{ ps}^{-1}$. Thus we assume that Γ does not follow the relation $\Gamma(n^*)^3 \approx \text{const.}$ along this Rydberg series. Γ following this relation would have been detectable when we determined the population decay rate constant since the decay rate would change by roughly a factor of three from $n = 10$ to $n = 13$.

On the basis of these simplifications it is possible to retrieve a coherent contribution to the photoelectron yield at least partly. We arrive at the fit curve to the data shown in Fig. 4(b). As one would expect on the basis of the restrictions made, the fit is only reasonable for the first part of the dependence of the photoelectron yield on the delay time. The reason for this is the rate constant damping the amplitudes of the coherent contributions to the photoelectron yield being the same as the rate constant $\Gamma = 4.6 \text{ ps}^{-1}$ for the population decay. The fit reveals that mainly the Fano resonance pair 142-144 (Table I) gives rise to a coherent contribution to the photoelectron yield. More details concerning this wave packet cannot reliably be extracted from the experimental data.

The analysis above did not take into account a possible coherent contribution to the photoelectron yield, which may stem from the substantial yield we find towards the end of the delay time interval in Fig. 4(b). It indicates that there have to be further Fano resonances contributing to the wave packet started by the harmonic H_{17} , which have substantially smaller population decay rate constants. These resonances do not show an obvious coherent contribution to the photoelectron yield in the delay time interval we investigated. The origin for this behavior may be either only one further resonance being involved, which has a small transition probability to the final state (after absorption of the IR photon), which is reached from the known resonances (Table I). Or more than one further resonance is involved with energy level spacings so small that a coherent contribution would not be detectable within the pump-probe delay range we have been able to investigate. This second scenario may apply since the bandwidth of the harmonic H_{17} spans the Xe ionization threshold identified as $5s^25p^4(^1D)5d(^2[4])$ in Ref. [20], thus possibly allowing the excitation of resonances corresponding to high Rydberg states ($n \gtrsim 20$) in a series converging at this threshold. From spectroscopy only the existence of the Fano resonances listed in Table I in the spectral range covered by the harmonic H_{17} is known. Our pump-probe experiment, however, indicates that there must be further resonances contributing within this spectral range, which have not been detected in spectroscopic investigations.

V. CONCLUSION

We investigated wave-packet dynamics in the ionization continuum of xenon in a spectral range where the continuum,

or more precisely the dipole transition matrix element from the atomic ground state to the continuum, is structured by Fano resonances. These Fano resonances are brought about by two-valence-electron and single-inner-valence-electron excited states, which are embedded in the ionization continuum. The evolution in time of such a wave packet is thus governed by two-electron dynamics, which eventually terminates in single ionization of the atom. In the spectral ranges investigated the wave packets launched encompassed many resonances, which are partly known from spectroscopic investigations. We tracked the evolution in time of the wave packets by inducing a continuum-continuum transition by a delayed infrared probe laser pulse and measuring the yield of photoelectrons, which absorbed an infrared photon. With this scheme we have been able to not only observe the autoionization dynamics of the wave packet but also to tentatively identify coherent contributions to the time evolution of the wave packets. A complete identification of the coherent content of the dynamics has to rely on the possibility to reach at least one final state after

absorption of the probe photon from all spectral components contributing to the wave packet with similar probabilities. If this is not possible there is only limited or possibly no access to the full dynamical evolution of the wave packet. Our results show that we only had limited access to the coherent part of the evolution in time of the wave packets we launched. One reason for this was the smallness of the oscillatory structure found on the photoelectron yield. A second one was the restricted delay time range we were able to access, a limitation, which will be overcome in future experiments. Our results indicate that the wave packet launched by the harmonic H_{17} in a spectral range well above the $5s5p^6$ ($^2S_{1/2}$) ionization threshold of Xe must contain contributions from resonances, which have not been found in spectroscopic experiments. A reason for this may be the dense resonance structure in this spectral range [19,23]. In energy ranges in the ionization continuum like this one the analysis of wave-packet motion may allow a deeper insight into the atomic spectral characteristics than spectroscopic methods have revealed up to now.

-
- [1] M. F. Kling and M. J. J. Vrakking, *Annu. Rev. Phys. Chem.* **59**, 463 (2008).
- [2] F. Krausz and M. Ivanov, *Rev. Mod. Phys.* **81**, 163 (2009).
- [3] M. Drescher, M. Hentschel, R. Kienberger, M. Uiberacker, V. Yakovlev, A. Scrinzi, T. Westerwalbesloh, U. Kleineberg, U. Heinzmann, and F. Krausz, *Nature (London)* **419**, 803 (2002).
- [4] O. Smirnova, V. S. Yakovlev, and A. Scrinzi, *Phys. Rev. Lett.* **91**, 253001 (2003).
- [5] C. Buth and K. J. Schafer, *Phys. Rev. A* **80**, 033410 (2009).
- [6] M. Wickenhauser, J. Burgdörfer, F. Krausz, and M. Drescher, *Phys. Rev. Lett.* **94**, 023002 (2005).
- [7] M. Wickenhauser, J. Burgdörfer, F. Krausz, and M. Drescher, *J. Mod. Opt.* **53**, 247 (2006).
- [8] Z. X. Zhao and C. D. Lin, *Phys. Rev. A* **71**, 060702 (2005).
- [9] W.-C. Chu and C. D. Lin, *Phys. Rev. A* **82**, 053415 (2010).
- [10] U. Fano, *Phys. Rev.* **124**, 1866 (1965).
- [11] B. Doughty, L. H. Haber, C. Hackett, and S. R. Leone, *J. Chem. Phys.* **134**, 094307 (2011).
- [12] B. Doughty, L. H. Haber, and S. R. Leone, *Phys. Rev. A* **84**, 043433 (2011).
- [13] H. Geiseler, H. Rottke, N. Zhavoronkov, and W. Sandner, *Phys. Rev. Lett.* **108**, 123601 (2012).
- [14] H. Wang, M. Chini, S. Chen, C.-H. Zhang, F. He, Y. Cheng, Y. Wu, U. Thumm, and Z. Chang, *Phys. Rev. Lett.* **105**, 143002 (2010).
- [15] C. Ott, A. Kaldun, P. Raith, K. Meyer, M. Laux, J. Evers, C. H. Keitel, C. H. Greene, and T. Pfeifer, *Science* **340**, 716 (2013).
- [16] B. Bernhardt, A. R. Beck, X. Li, E. R. Warrick, M. J. Bell, D. J. Haxton, C. W. McCurdy, D. M. Neumark, and S. R. Leone, *Phys. Rev. A* **89**, 023408 (2014).
- [17] J. E. Thoma and R. R. Jones, *Phys. Rev. Lett.* **83**, 516 (1999).
- [18] H. Geiseler, H. Rottke, G. Steinmeyer, and W. Sandner, *Phys. Rev. A* **84**, 033424 (2011).
- [19] K. Codling and R. P. Madden, *Phys. Rev. A* **4**, 2261 (1971); *J. Res. Nat. Bur. Stand.* **76A**, 1 (1972).
- [20] A. Kramida, Y. Ralchenko, J. Reader, and N. A. Team, Nist atomic spectra database (ver. 5.1) (2013), <http://physics.nist.gov/asd>.
- [21] V. L. Sukhorukov, I. D. Petrov, B. M. Lagutin, H. Schmoranzner, W. Kielich, P. V. Demekhin, and A. Ehresmann, *Eur. Phys. J. D* **59**, 151 (2010).
- [22] J. E. Hansen and W. Persson, *Physica Scripta* **36**, 602 (2011).
- [23] M. Ukai, N. Terazawa, Y. Chikahiro, K. Kameta, N. Kouchi, Y. Hatano, and K. Tanaka, *Phys. Rev. A* **45**, R15(R) (1992).
- [24] P. M. Paul, E. S. Toma, P. Breger, G. Mullot, F. Augé, P. Balcou, H. G. Muller, and P. Agostini, *Science* **292**, 1689 (2001).
- [25] D. L. Ederer, *Phys. Rev. A* **4**, 2263 (1971); **14**, 1936 (1976).